Reconfigurable, non-volatile neuromorphic photovoltaics

Tangxin Li
State Key Laboratory of Infrared Physics
Jinshui Miao
Shanghai Institute of Technical Physics, Chinese Academy of Sciences https://orcid.org/0000-0002-3041-1105
Xiao Fu
State Key Laboratory of Infrared Physics
Bo Song
Institute of Intelligent Machines
Bin Cai
Institute of Intelligent Machines
Xiaohao Zhou
Shanghai Institute of Technical Physics,Chinese Academy of Sciences
Peng Zhou
Fudan University https://orcid.org/0000-0002-7301-1013
Xinran Wang
Nanjing University https://orcid.org/0000-0002-3975-1667
Deep Jariwala (dmj@seas.upenn.edu)
The University of Pennsylvania https://orcid.org/0000-0002-3570-8768
Weida Hu
Shanghai Institute of Technical Physics, Chinese Academy of Sciences https://orcid.org/0000-0001-5278-8969

Article

Keywords:

Posted Date: February 21st, 2023

DOI: https://doi.org/10.21203/rs.3.rs-2558516/v1

Version of Record: A version of this preprint was published at Nature Nanotechnology on July 20th, 2023. See the published version at https://doi.org/10.1038/s41565-023-01446-8.

Abstract

Reconfigurable image sensors for the recognition and understanding of real-world objects are now becoming an essential part of machine vision technology. The neural network image sensor — which mimics neurobiological functions of the human retina —has recently been demonstrated to simultaneously sense and process optical images. However, highly tunable responsivity concurrently with non-volatile storage of image data in the neural network would allow a transformative leap in compactness and function of these artificial neural networks (ANNs) that truly function like a human retina. Here, we demonstrate a reconfigurable and non-volatile neuromorphic device based on two-dimensional (2D) semiconducting metal sulfides (MoS_2 and WS_2) that is concurrently a photovoltaic detector. The device is based on a metal/semiconductor/metal (M/S/M) two-terminal structure with pulse-tunable sulfur vacancies at the M/S junctions. By modulating sulfur vacancy concentrations, the polarities of short-circuit photocurrent —can be changed with multiple stable magnitudes. Device characterizations and modeling reveal that the bias-induced motion of sulfur vacancies leads to highly reconfigurable responsivities by dynamically modulating the Schottky barriers. A convolutional neuromorphic network (CNN) is finally designed for image process and object detection using the same device. The results demonstrated the two-terminal reconfigurable and non-volatile photodetectors can be used for future optoelectronics devices based on coupled Ionic-optical-electronic effects for Neuromorphic computing.

Introduction

The use of sensory nodes in neuromorphic vision networks is on the rise, but the data generated by these nodes are often unstructured and redundant for machine-learning algorithms[1]. This is because the sensory units, which operate mostly in the analog domain, are physically separate from the processing units, which are typically executed digitally using von Neumann architecture. As a result, large amounts of data must be transferred to local processing units or cloud-based systems, leading to high energy consumption, latency, insufficient storage space, and communication bandwidth[2]. In contrast, the human visual system can perform complex tasks in real-time due to its inherent parallelism, which allows for the combination of image sensing and processing functions[3–5].

To address this issue, researchers have developed retina-inspired devices based on bulk materials and two-dimensional (2D) materials, such as variable-sensitivity photodetectors (VSDP)[6, 7], dual-gate photodiodes (DGP)[8, 9], two-terminal photo-memories (TPM)[10–14], and gate-tunable vision sensors (GVS)[15–22]. However, these neural network sensors often suffer from bias-dependent dark current with high power consumption (VSDP), volatile photocurrent for neural network (TPM), or complicated preparation process for integration and low photoresponsivity (DGP, GVS). In this context, 2D materials offer superior features for neuromorphic vision hardware, since they show strong light-matter interaction in a broad part of the spectrum[23], ease of fabrication and integration[24, 25], as well as the possibility of static and dynamic tunability of the potential profile within a device[26–28]. Further, 2D materials as a

technology are now advanced and mature enough to be used over wafer scales in complex integrated device and circuit level systems which can further be easily integrated with silicon readout/control electronics[29–34].

In this study, we present a two-terminal photovoltaic detector based on metal/2D-semiconductor/metal (M/S/M) structures using layered metal sulfides (MoS2, WS2) as the 2D semiconductors. By artificially introducing sulfur vacancies (positive ions) and controlling their migration with an electric field (voltage pulses), we can change the local sulfur ion concentration and adjust the Schottky barrier height at the M/S junction regions. This scheme not only allows for the adjustment of multiple resistance states in the 2D M/S/M photodetectors, mimicking biological synapses, but also the sign of the net photocurrent. The increase/decrease of Schottky barrier height in the two-terminal photodetector can break the symmetry of electric potential in the M/S/M devices, leading to change in sign of the photocurrent and even achieving zero photocurrent at zero bias. Overall, this allows for tuning the amplitude and polarity of zero-biased photocurrent with non-volatile responsivities, which when applied to neuromorphic vision networks, greatly simplifies the architecture for object position detection.

Device Fabrication And Architecture

The device fabrication process involves transferring a mechanically exfoliated 2D MoS2 flake of approximately 10 nm thickness (Supplementary Information Fig. 1) onto SiO2/p + + Si substrates. Standard microfabrication processes were then used to fabricate the source/drain (S/D) electrodes. It is important to note that the 2D MoS2 under the S/D metal electrodes is treated with argon/oxygen plasma, which leaves a high concentration of sulfur vacancies (ions) at the M/S junction regions. The MoS2 photodetector has two M/S Schottky diodes connected back-to-back, as shown in Fig. 1a. Scanning electron microscopy (SEM) images (Fig. 1b) show the 2D-MoS2 M/S/M photodetector where the MoS2 under the S/D electrodes is treated with plasma, while the MoS2 channel (~ 1 μm) is untreated. To further characterize the device, we used Raman spectrum and transmission electron microscopy (TEM) to analyze the pristine and plasma-treated MoS2. A redshift of $E_{2g}{}^{1}$ peak and a blue shift of A_{1g} peak, indicating a change in MoS2 thickness with plasma treatment (Supplementary Information Fig. 2) was observed. Cross-sectional TEM and corresponding energy dispersive spectroscopy (EDS) analysis confirmed the presence of rich sulfur vacancies (positive ions) introduced by plasma treatment.

Wavelength-dispersive X-ray spectroscopy (WDS) was used to analyze the distribution of sulfur atoms and molybdenum atoms in the channel and below the S/D electrode. We observe a contrast ratio of 1.95 of sulfur atoms to molybdenum atoms in the channel and a ratio of 1.42 below the S/D electrodes, indicating the presence of sulfur vacancies after plasma treatment (Supplementary Information Fig. 3). X-ray photoelectron spectroscopy also confirms that the S/Mo atomic ratio of pristine MoS2 is 1.94 while the S/Mo atomic ratio of plasma treated MoS2 is reduced to 1.50, further indicating the absence of sulfur atoms (Supplementary Information Fig. 4). Additional device fabrication and structural characterization is detailed in Methods. Figures 1e and 1f show the dynamic photocurrent characteristics of the two-terminal MoS2 photodetectors with plasma-treated M/S junctions. The MoS2 photodetector initially

shows an obvious photovoltaic effect with short-circuit current (I_{sc}) of + 10 nA and open-circuit voltage (V_{oc}) of -6 mV under 532 nm light illumination (Fig. 1e). However, after 15 V pulses of 10 s duration, the MoS2 photodetector shows opposite photocurrent behaviors with I_{sc} of -13 nA and V_{oc} of -8 mV under the same biasing conditions (Fig. 1f). In Figs. 1g, 1h and Supplementary Information Fig. 5, The time-resolved photocurrent further demonstrates its tunable polarity in the visible to infrared regions (Fig. 1g, h and Supplementary Information Fig. 5). The tunable polarity in I_{sc} is also observed in other metal sulfides like WS2 (Supplementary Information Fig. 6). However, for the pristine MoS2 M/S/M device (untreated with plasma), the photocurrent has no obvious change upon application of same magnitude and duration of voltage pulses, (Supplementary Information Fig. 7). The tunable photocurrent by voltage pulses is mainly attributed to the migration of sulfur vacancies by the electric field and strong ion-electron coupling.

Dynamic Photocurrent Characteristics

The dynamic photocurrent characteristics of the device were studied using a two-terminal M/S/M configuration, with one electrode as an anode and another as a cathode. We collected multiple and non-volatile photocurrent states (I_{sc}) by applying a constant light intensity under short-circuit conditions. To investigate the tunable polarity and amplitude of the photocurrent state, we conducted scanning photocurrent measurements by scanning the laser spot across the anode, channel, and cathode (Fig. 2 and Supplementary Information Figure 8). As shown in Fig. 2a-i and Fig. 2a-iv, the photoresponse, without applying any voltage pulses, is locally observed at the metal/MoS2 contact (dashed square) with similar amplitude but opposite signs — where the photocurrent at the anode is positive while the photocurrent at the cathode is negative. However, after voltage pulse programming (15 V and 15 s duration), the same device shows enhanced positive photocurrent at the anode, while the negative photocurrent at the cathode almost vanishes, as shown in Fig. 2a-ii. Further, the same device after voltage pulse programming with reversed sign but same amplitude (-15 V and 15 s duration) shows opposite photocurrent behavior i.e. the negative photocurrent at the cathode is enhanced while the positive photocurrent at the anode almost vanishes, as shown in Fig. 2a-iii. To further confirm this reconfigurability, the 15V 15s voltage pulse is again applied to the same device with a photocurrent state as shown in Fig. 2-iii, and the photocurrent is fully recovered to its initial state as shown in Fig. 2a-i (similar amplitude but opposite signs, Supplementary Information Figure 9). Fig. 2a-iv shows the corresponding photocurrent amplitude as a function of laser spot position extracted from Figs. 2a-i, ii, iii. Note that the volage pulsing can effectively modulate the amplitude and polarity of local photocurrent at the M/S junctions. Fig. 2b shows the photocurrent map of pristine MoS2 M/S/M photodetector without plasma treatment and the photocurrent amplitude at the M/S junction shows negligible changes even with multiple voltage pulse programming. Further, the amplitude of photocurrent of pristine device (~ pA) is much lower than the plasma treated device (~ mA). This experiment shows that the migration of sulfur vacancies (ions) strongly affects the photocurrent amplitude and polarity of the plasma-treated MoS2 photodetector. This is due to the ion-electron coupling effect. Fig. 2c illustrates the I-V characteristics of the plasma-treated MoS2 photodetector in the dark and under global illumination. Initially, the device

shows an I_{sc} of -6 nA and a V_{oc} of 5 mV (black line, left of Fig. 2c). However, after many rounds of voltage pulse programming (-15/-20 V, 100 ms, +50/100 pulse), the device ultimately shows opposite I-V behavior with an I_{sc} of 50 nA and a V_{oc} of -25 mV. Similarly, a device with an I_{sc} of 50 nA and a V_{oc} of 10 mV (black line, right of Fig. 2c) can be ultimately modulated to an opposite I-V behavior with an I_{sc} of 50 nA and a V_{oc} of -25 mV after voltage pulse programming (15 V, 100 ms, +400/700 pulse). In contrast, for pristine MoS2 devices, no obvious photovoltaic effect was observed after many rounds of voltage pulse programming (Fig. 2d). The plasma-treated MoS2 devices further show six states of I_{sc} and V_{oc} by varying the duration of the voltage pulses (Supplementary Information Figure 10).

It is important to note that this phenomenon is not observed in a one-off device and has been highly reproducible in many devices as shown in the statistical chart (Fig. 2f and Supplementary Information Figure 11).

Ion Modulation And Ionic Coupling Effect

To understand the atomic mechanism behind the reconfigurable and non-volatile responsivity of MoS2 M/S/M devices, we conducted a series of experiments using WDS characterizations, Kelvin probe force microscope (KPFM), and Sentaurus-TCAD simulation. We observed the in-situ distribution of sulfur atoms in the MoS2 channel by applying voltage biases to the M/S contact, creating an in-plane electric field of approximately 10 MV/cm. Our results, shown in Fig. 3a, revealed that before applying voltage pulses, the sulfur atoms were uniformly distributed across the channel. The red signal in WDS map shows the distribution of sulfur atoms in the channel. From Fig. 3a-i and Fig. 3a-ii, the WDS map and corresponding elemental spectrum demonstrate uniform sulfur distribution across the MoS2 channel before electric pulse programming. However, after applying a negative voltage pulsing (amplitude, -10 V; duration, 10 s) on anode (with cathode grounded, Fig. 3b-i), the MoS2 channel shows the obvious absence of sulfur atoms near anode indicating the migration of sulfur vacancies. In Fig. 3b-ii, the intensity of sulfur atoms near the anode is lower than the intensity of sulfur atoms near the cathode.

To demonstrate the reversible migration of sulfur vacancies, positive (amplitude, + 10 V; duration, 10 s) electric pulses are applied to anode in sequence; the MoS2 channel restoring to its initial uniform sulfur distribution indicating the reversible migration of sulfur ions (Fig. 3c-i). And the uniform distribution of sulfur atoms is observed in elemental spectrum as shown in Fig. 3c-ii. The device schematics illustrate the sulfur atom migration near anode and cathode (Fig. 3a-iii, Fig. 3b-iii and Fig. 3c-iii). After the positive/negative electric pulses, the distribution of sulfur atom changes the ions density at anode and cathode. Since the layered MoS2 offers ionic pathways with low activation energy, the sulfur ions have a high in-plane diffusivity[35, 36]. Therefore, the sulfur ion migration in the MoS2 channel, driven by an electric field, modifies the local sulfur concentration. The increase/decrease in the local S ion concentration leads to the dynamic decrease/increase of Schottky barrier height[37, 38]. The asymmetric Schottky barrier of M/S contact can facilitate the separation of photo-generated electron-hole pairs due to the potential gradient leading to a large I_{sc}. Moreover, like memristors, the multiple photocurrent states are

non-volatile because the barrier is modulated by ion concentration which remains fixed in the absence of a large electric field. The asymmetric distribution of sulfur ions in the MoS2 channel results in a strong photovoltaic effect with a maximum I_{sc} of -795 nA and V_{oc} of 60 mV (Supplementary Information Fig. 12). Also, the maximum optical responsivity of 369.22 mA/W was achieved with ionic migration.

We further conducted KPFM measurements (to map the magnitude and potential of MSM device, Fig. 3d) verifying the dynamic modulation of the Schottky barrier at the metal/MoS2/metal junction with various voltage programming conditions. The results, shown in Fig. 3e, indicated that the Schottky barrier height at the anode region (high sulfur vacancy concentration) was lower than that at the cathode region (low sulfur vacancy concentration), with a difference of approximately 50 meV. In contrast, the pristine MoS2 device displayed a symmetric Schottky barrier (Supplementary Information Fig. 13). These results were consistent with the WDS maps, which showed that a negative voltage applied to the anode attracts sulfur vacancies towards the anode and reduces the number of vacancies near the cathode, leading to the formation of Schottky or Ohmic contact at the metal/MoS2 interface and affecting the observed I_{sc} and V_{oc}. To further understand the impact of the asymmetric Schottky barrier on photocurrent, we used Sentaurus-TCAD to simulate the band structure, electric field distribution, and photocurrent response of the metal/MoS2/metal device. The simulated band structure, shown in Fig. 3f, displayed the potential gradient induced by the asymmetric Schottky barrier. Figure 3g also showed an obvious I_{sc} due to the asymmetric Schottky barrier. The simulated electron density distribution with different barrier at anode and cathode under illumination are shown in Supplementary Information Fig. 14. The lower anode barrier corresponds to the larger I_{sc}, confirming the experiment results.

Overall, our theoretical and experimental results discussed above demonstrate that the reconfigurable and non-volatile responsivity of M/S/M photodetectors is due to the electric field-driven redistribution of sulfur vacancies, which dynamically changes the Schottky barrier and doping profile.

Reconfigurable Neuromorphic Sensing

With the above described reconfigurable and non-volatile photovoltaic response in the 2D M/S/M device, a convolutional neuromorphic network (CNN) is designed and demonstrated for image processing and classification[15, 20]. The responsivity and conductance of our device are programmed to perform the multiply-accumulation (MAC) operation for the CNN. Here, a more complex CNN task – object detection – has been realized. In order to achieve high accuracy, we utilized eleven non-volatile responsivity states with varying I_{sc} polarities as depicted in Fig. 4a. And the linear interval of short-circuit current reaches 4000 mW/cm^2 .The temporal photocurrent response and calculation of the responsivity states are illustrated in Supplementary Information Figs. 15 and 16. Additionally, the I_{sc} was found to change linearly with the optical power density, which is crucial for updating the weight in the neuromorphic network, as shown in Fig. 4b. The specific pulse numbers and duration for the eleven responsivity states can be found in Fig. 4c. These responsivity states were found to be stable and maintain their integrity for longer than 1000 seconds, as demonstrated in Supplementary Information Fig. 17. Using these multiple

responsivity states, we were able to successfully demonstrate image processing for "Cameraman," "Lena," and "Peppers" and image classification for MNIST "0–9" as seen in Supplementary Information Figs. 18 and 19. Furthermore, we examined the tunable conductance in 2D M/S/M devices by applying multiple electric pulses, which resulted in reconfigurable conductivity for up to 168 conductivity states, as shown in Supplementary Information Fig. 20.

Object detection is a more challenging task for convolutional neural networks (CNNs) than image classification, as it requires precise computation of localization parameters[39]. Conventional object detection models typically require direct regression of the coordinates of the top-left corner (r,c) or the object center (x,y) and its height and width (h,w)[40, 41]. However, these models can struggle when applied to systems with limited programmed states (both optically and electrical states), which can lead to inaccurate regression results or failures. To address this problem, we proposed a unified discrete weight object detection framework for object center detection that is able to accommodate the limited discrete levels of the programmable states in our devices, as shown in Fig. 4d. Our networks only contain convolution layers and activation operations, without BatchNorm or InstanceNorm operations. Discretization operations were applied to the weights in the offline-trained network to adapt to the limited discrete levels of our programmable states. The training strategies and the OSU Thermal Pedestrian Database used for object detection are presented in Supplementary Information Figs. 21 and 22. Instead of directly regressing the coordinates of the object center, our unified discrete weight object detection network generates a heatmap for object detection, with peaks in the heatmap corresponding to object centers. The position of the maximum value in the heatmap will not be affected after weight discretization. After training, we obtained a heatmap with 24x24 pixels for the calculation of the target position. We then employed a 24x24 memristor array to display the 24x24-pixel image. Through Ohm's law and multiply-accumulate processing[42], the maximum row and column voltage values can be obtained (Fig. 4e). The detected (x,y) coordinate location of the object image can be displayed by the maximum voltage in the memristor array (Supplementary Information Fig. 23).

Finally, we compared the performance of object detection network with three types of weights, namely float-16 datatype weights, weight discretization only in the optical network, weight discretization in both the optical and electronic networks. The accuracy of object detection, for our 11 responsivity states in optical front-end with float-16 weights in electronic processing is ~ 97% and for our 11 responsivity states in optical front-end with our conductivity states in electronic processing is ~ 96% as shown in Fig. 4f. And the loss of three types of weights decreases in ~ 10 epochs and converges to ~ 50 epochs in Fig. 4g. These experimental results showed that the performance of our discrete weight framework is comparable with the float-16 datatype network.

Conclusion

In summary, we have presented reconfigurable and non-volatile photovoltaic-detector devices for intelligent image processing and object detection. The devices are based on a simple two-terminal M/S/M architecture with 2D semiconducting metal sulfides as the channel. The migration of sulfur

vacancies driven by electric pulses lead to the modulation of M/S Schottky barrier due to the electron-ion coupling effect. The magnitude and polarity of device responsivity are highly tunable and non-volatile which can be used to build neuromorphic hardware for intelligent perception as demonstrated. Furthermore, scaling the neuromorphic hardware to larger dimensions is conceptually feasible due to the simple device structure and provides various training possibilities for neuromorphic vision applications.

Methods

Device fabrication. Multi-layer MoS_2 flakes were mechanically exfoliated from the high- quality bulk crystal (HQ Graphene, Netherlands) onto the polydimethylsiloxane (PDMS) and transferred onto a silicon substrate with 300nm SiO_2 (Universitywafer, America). Then, the electrode patterns were defined by the electron-beam lithography (EBL). After that, the positions of electrode patterns were exposed to O_2 and Ar plasma in the Precision Soft Etching System (nanoETCH), while the MoS_2 channel was protected by a photolithography-patterned photoresist. For O_2 or Ar plasma treatment process, the etch power was set to 10 W, the chamber pressure is 1×10^{-7} Torr, the gas flow rate was 30 sccm. O_2 and Ar processing times were 10 s and 30 s, respectively. Finally, the 1 nm Cr and 50 nm Au layers were deposited on MoS2 by thermal evaporation with a base pressure of 3×10^{-6} Torr and a deposition rate of 0.3 Å s^{-1}, followed by the standard lift-off process.

WDS measurements. WDS measurements of the M/S/M devices were carried out by a unique wavelength-dispersive soft X-ray emission spectrometer in an electron probe micro analyzer (EPMA) equipped with a Schottky field emission (FE) electron gun, which is designed to enhance the analytical area of nanometers in size.

TEM imaging and EDS mapping. Samples were treated with plasma and evaporated 10nm Au for protection immediately. For TEM, samples were prepared using a Thermo Scientific Helios G4 HX dual-beam system. The samples were covered by a carbon layer deposited using electron-beam evaporation and a thicker platinum protective layer was deposited using sputtering. TEM imaging was conducted in a Thermo Scientific Tecnai F20 (200kV) transmission electron microscope. We also got the distribution of elements from the EDS mapping in our materials.

Raman and XPS measurements. Raman spectra were obtained by using a Lan Ram HR800 with a 532 nm laser as an excitation source. XPS characterizations were using a PHI5000 VersaprobeIII system that base pressure was 4×10^{-8} Torr. The source was operated at 15 kV with an emission current of 4.5 mA.

AFM and KPFM measurements. The thickness and surface potential of our device were characterized by a scanning probe microscope (Cypher S).The KPFM measurements were using a tip coated with Ti/Ir thin film (ASYELEC-01-R2) in the SKPM mode at 0 bias voltage. And the AFM imaging was acquired from the height retrace mode in the KPFM testing process.

Device characterization. The electrical characterizations of the devices were conducted using a commercial Keysight B1500A in a Lake Shore probe station. The devices were wire-bonded onto a 28-pin printed circuit board (PCB) and 520 nm, 830 nm laser was used for photoresponse measurements. The devices was positioned at the central of the light spot to make sure a uniform illumination. The data of response time was acquired using a Textronix MDO3014 oscilloscope. All the measurements were carried out at room temperature in an ambient environment.

TCAD simulations. Simulations of metal/MoS_2/metal device under illumination conditions were performed using Sentaurus TCAD from Synopsys Inc. The model of the device and additional details were discussion in the Supplementary Information.

Declarations

Data availability

The data that support the conclusions of this study are available from the corresponding authors upon reasonable request. Source data are provided with this paper.

Code availability

The codes used for simulation and data plotting are available from the corresponding authors upon reasonable request.

Acknowledgements

This work was supported by the National Key Research and Development Program of China (2021YFA0715602), the National Natural Science Foundation of China (62261136552, 62005303, and 62134001), the International Partnership Program of Chinese Academy of Sciences (Grant No. 181331KYSB20200012), the Science and Technology Commission of Shanghai Municipality (21JC1406100), the Alfred P. Sloan Foundation (Sloan Fellowship in Chemistry) (D.J.), the Open Research Projects of Zhejiang Lab (2022NK0AB01).

Author contributions

J. M., D. J., and W. H. conceived the idea/concept and directed the collaboration and execution. T.L. and X.F. fabricated the devices and performed the measurements. T.L., J. M., P.Z., X. W., D.J., and W. H. analyzed the experimental data. T. L. X. Z., and J. M. did the TCAD device simulation. B.S. and B.C. performed the AI object detection. T. L., J.M., W. H., and D.J. co-wrote the manuscript with contributions

from all the authors. All authors discussed the results and implications and commented on the manuscript at all stages.

Competing interests

The authors declare no competing interests.

References

1. Sze, V., Yu-Hsin, C., Emer, J., Suleiman, A.&Zhengdong, Z. Hardware for machine learning: challenges and opportunities. *In* 2017 *IEEE Custom Integrated Circuits Conference (CICC)* 179–186 (IEEE, 2017)
2. Zhou, F.&Chai, Y. Near-sensor and in-sensor computing Nat. Electron. **3**, 664–671 (2020).
3. Gollisch, T.&Meister, M. Eve Smarter than Scientists Believed: Neural Computations in Circuits of the Retina *Neuron* **65**, 150–164 (2010).
4. Kyuma, K., et al. ARTIFICIAL RETINAS - FAST, VERSATILE IMAGE-PROCESSORS Nature **372**, 197–198 (1994).
5. Kolb, H. How the retina works - Much of the construction of an image takes place in the retina itself through the use of specialized neural circuits Am. Scientist **91**, 28–35 (2003).
6. Funatsu, E., et al. An artificial retina chip with current-mode focal plane image processing functions IEEE Trans. Electron Devices **44**, 1777–1782 (1997).
7. Nitta, Y., Ohta, J., Tai, S.&Kyuma, K. Variable-sensitivity photodetector that uses a metal-semiconductor-metal structure for optical neural networks Opt. Lett. **16**, 611–613 (1991).
8. Jang, H., et al. In-sensor optoelectronic computing using electrostatically doped silicon Nat. Electron. **5**, 519–525 (2022).
9. Mennel, L., et al. Ultrafast machine vision with 2D material neural network image sensors *Nature* **579**, 62–66 (2020).
10. Chen, S., Lou, Z., Chen, D.&Shen, G. An Artificial Flexible Visual Memory System Based on an UV-Motivated Memristor Adv. Mater. **30**, (2018).
11. Cui, B., et al. Ferroelectric photosensor network: an advanced hardware solution to real-time machine vision Nat. Commun. **13**, (2022).
12. Sun, L., et al. In-sensor reservoir computing for language learning via two-dimensional memristors Sci. Adv. **7**, eabg1455 (2021).
13. Zhou, F., et al. Optoelectronic resistive random access memory for neuromorphic vision sensors Nat. Nanotechnol. **14**, 776–782 (2019).
14. Ahmed, T., et al. Optically Stimulated Artificial Synapse Based on Layered Black Phosphorus Small **15**, (2019).
15. Lee, S., Peng, R., Wu, C.&Li, M. Programmable black phosphorus image sensor for broadband optoelectronic edge computing Nat. Commun. **13**, 1485 (2022).

16. Liao, F., et al. Bioinspired in-sensor visual adaptation for accurate perception Nat. Electron. **5**, 84–91 (2022).
17. Liu, K., et al. An optoelectronic synapse based on α-In2Se3 with controllable temporal dynamics for multimode and multiscale reservoir computing Nat. Electron. **5**, 761–773 (2022).
18. Pi, L., et al. Broadband convolutional processing using band-alignment-tunable heterostructures Nat. Electron. **5**, 248–254 (2022).
19. Seo, S., et al. Artificial optic-neural synapse for colored and color-mixed pattern recognition Nat. Commun. **9**, 5106 (2018).
20. Wang, C.-Y., et al. Gate-tunable van der Waals heterostructure for reconfigurable neural network vision sensor Sci. Adv. **6**, eaba6173 (2020).
21. Yu, J., et al. Bioinspired mechano-photonic artificial synapse based on graphene/MoS2 heterostructure Sci. Adv. **7**, eabd9117 (2021).
22. Zhang, Z., et al. All-in-one two-dimensional retinomorphic hardware device for motion detection and recognition Nat. Nanotechnol. **17**, 27–32 (2022).
23. Lien, D.-H., et al. Engineering Light Outcoupling in 2D Materials Nano Lett. **15**, 1356–1361 (2015).
24. Wang, Q. H., Kalantar-Zadeh, K., Kis, A., Coleman, J. N.&Strano, M. S. Electronics and optoelectronics of two-dimensional transition metal dichalcogenides Nat. Nanotechnol. **7**, 699–712 (2012).
25. Shim, J., et al. Controlled crack propagation for atomic precision handling of wafer-scale two-dimensional materials *Science* **362**, 665–670 (2018).
26. Khan, M. A., et al. The non-volatile electrostatic doping effect in MoTe2 field-effect transistors controlled by hexagonal boron nitride and a metal gate Sci Rep **12**, 12085 (2022).
27. Wang, M., et al. Robust memristors based on layered two-dimensional materials Nat. Electron. **1**, 130–136 (2018).
28. Zhu, X., Li, D., Liang, X.&Lu, W. D. Ionic modulation and ionic coupling effects in MoS2 devices for neuromorphic computing Nat. Mater. **18**, 141–148 (2019).
29. Chen, H., et al. Logic gates based on neuristors made from two-dimensional materials Nat. Electron. **4**, 399–404 (2021).
30. Liu, W., et al. Graphene charge-injection photodetectors Nat. Electron. **5**, 281–288 (2022).
31. Tong, L., et al. 2D materials-based homogeneous transistor-memory architecture for neuromorphic hardware *Science* **373**, 1353–1358 (2021).
32. Wang, Y., et al. An in-memory computing architecture based on two-dimensional semiconductors for multiply-accumulate operations Nat. Commun. **12**, (2021).
33. Miao, J., et al. Heterojunction tunnel triodes based on two-dimensional metal selenide and three-dimensional silicon Nat. Electron. **5**, 744–751 (2022).
34. Choi, C., et al. Human eye-inspired soft optoelectronic device using high-density MoS2-graphene curved image sensor array Nat. Commun. **8**, (2017).

35. Duy, L., Rawal, T. B.&Rahman, T. S. Single-Layer MoS2 with Sulfur Vacancies: Structure and Catalytic Application J. Phys. Chem. C **118**, 5346–5351 (2014).
36. Komsa, H.-P., Kurasch, S., Lehtinen, O., Kaiser, U.&Krasheninnikov, A. V. From point to extended defects in two-dimensional MoS2: Evolution of atomic structure under electron irradiation Phys. Rev. B **88**, (2013).
37. Li, D., et al. MoS2 Memristors Exhibiting Variable Switching Characteristics toward Biorealistic Synaptic Emulation Acs Nano **12**, 9240–9252 (2018).
38. Sangwan, V. K., et al. Multi-terminal memtransistors from polycrystalline monolayer molybdenum disulfide Nature **554**, 500–504 (2018).
39. Xingyi, Z., Koltun, V.&Krahenbuhl, P. Tracking Objects as Points. *Computer Vision - ECCV 2020. 16th European Conference* 474–490 (2020)
40. Redmon, J., Divvala, S., Girshick, R., Farhadi, A.&Ieee You Only Look Once: Unified, Real-Time Object Detection. *In* 2016 *IEEE Conference on Computer Vision and Pattern Recognition (CVPR)* 779–788 (IEEE, 2016)
41. Ren, S., He, K., Girshick, R.&Sun, J. Faster R-CNN: Towards Real-Time Object Detection with Region Proposal Networks. *In 29th Annual Conference on Neural Information Processing Systems (NIPS)* (2015)
42. Ielmini, D.&Wong, H. S. P. In-memory computing with resistive switching devices Nat. Electron. **1**, 333–343 (2018).

Figures

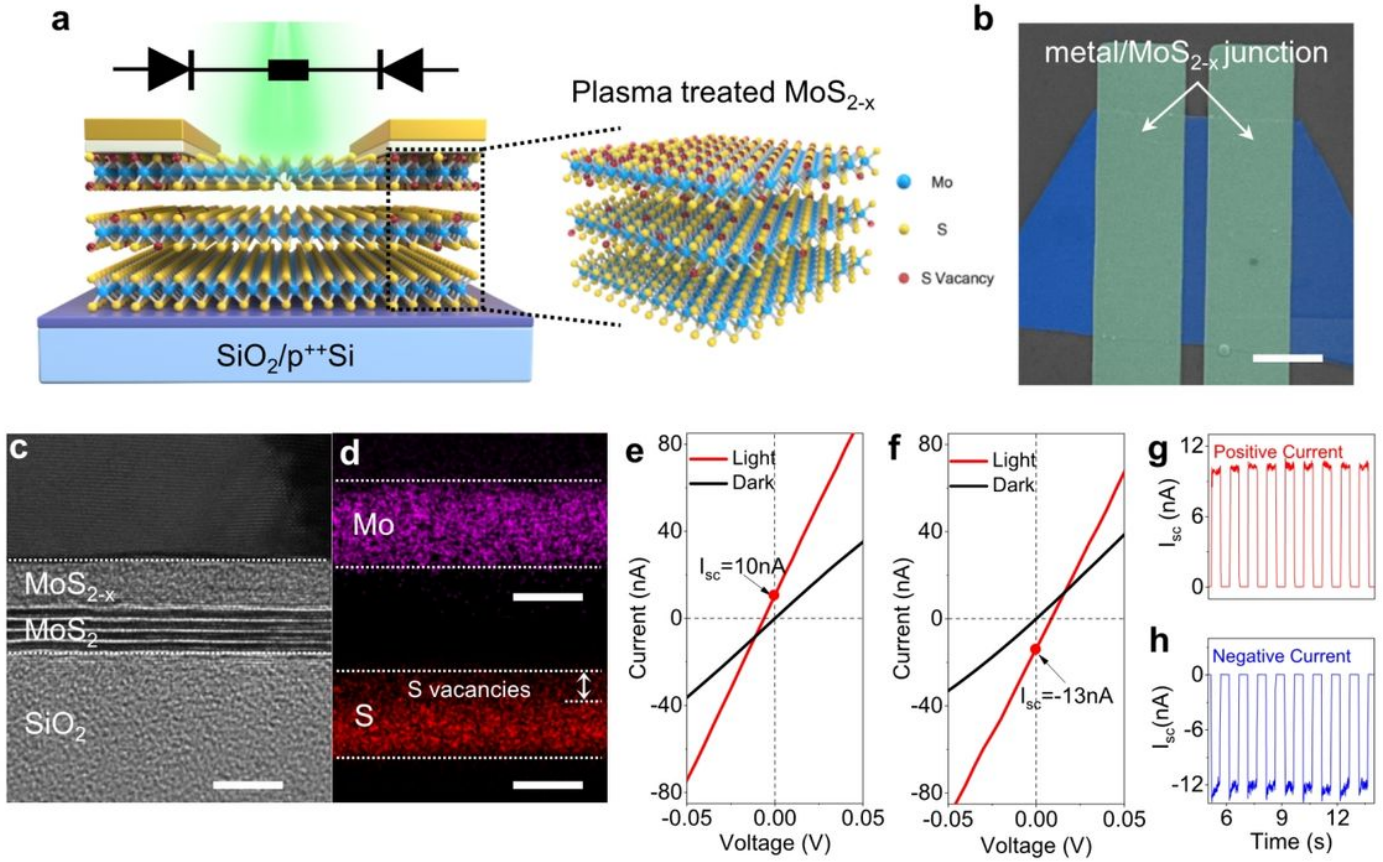

Figure 1. Device characterizations of the plasma-treated MoS_2 M/S/M photovoltaic detectors. a, Schematic of the M/S/M device structure with M/S Schottky diodes connected back to back. The MoS_2 under the S/D electrodes is treated with plasma. Blue sphere: molybdenum, yellow sphere: sulfur, red sphere: sulfur vacancy. **b**, False-colored SEM image of a MoS_2 M/S/M photovoltaic detector, the green, and blue regions represent M/S junctions and MoS_2 flake, respectively. Scale bar, 4 μm. **c**, Cross-sectional TEM images of the MoS_2 under the electrode showing MoS_{2-x} and MoS_2 layer. Scale bar, 2 μm. **d**, EDS map of plasma treated MoS_2 layer in panel **c**, where the S atoms are depleted at the metal/MoS_2 interface. **e, f** Typical I-V characteristics of the M/S/M reconfigurable photovoltaic detector before (e) and after (f) applying a pulse of 15V for 10s, the short-circuit current (I_{sc}) switches from 10 nA to -13 nA in a non-volatile mode. **g, h**, Temporally resolved photocurrent response under V_{ds}=0V, λ=520nm of **e** and **f**.

Figure 1

See above image for figure legend.

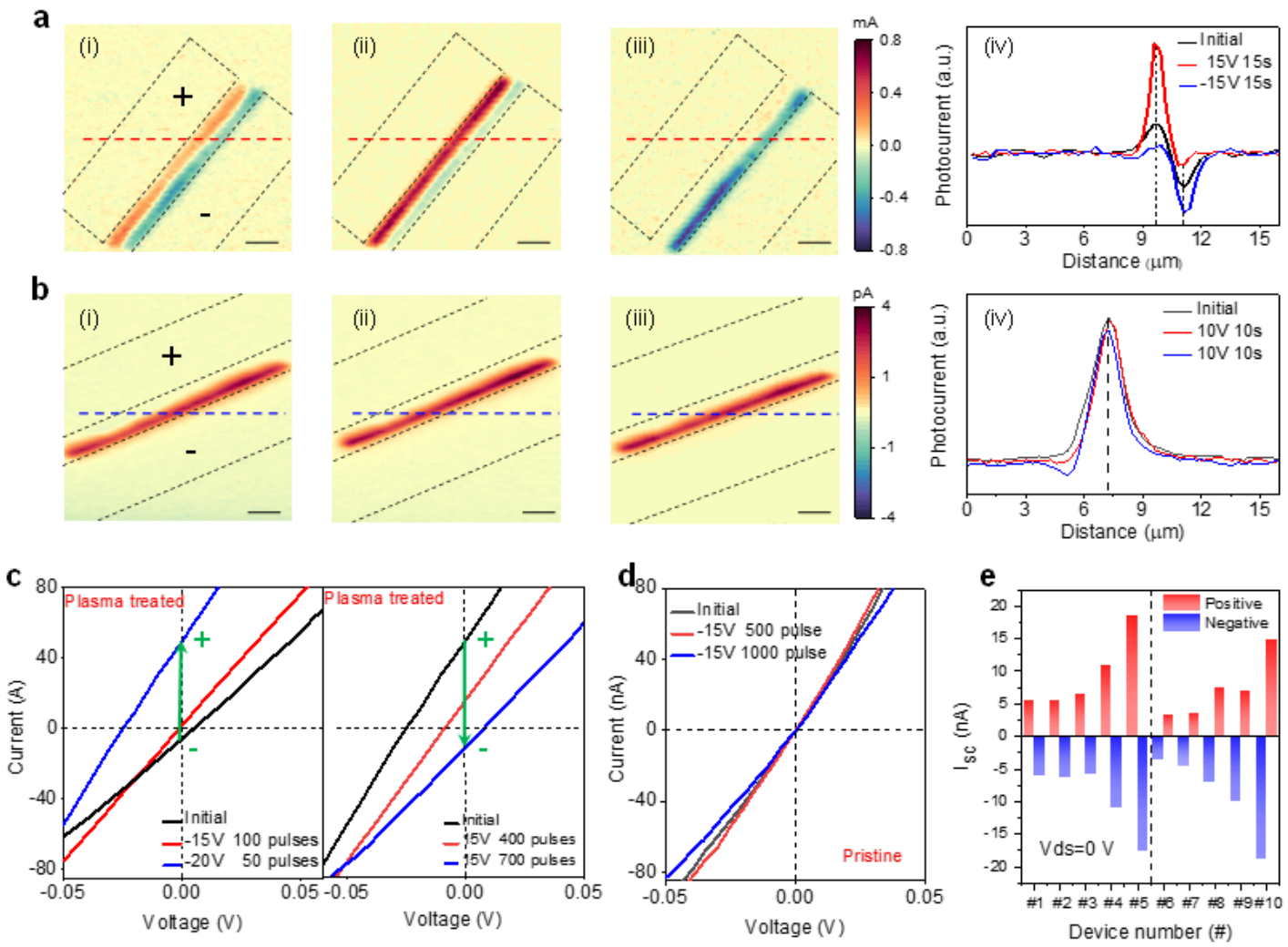

Figure 2

Photocurrent mapping and pulse programmable characteristics of plasma-treated and pristine MoS_2 M/S/M devices. a, b Photocurrent mapping of the MSM photovoltaic detector with **(a)** and without **(b)** plasma treatment at the initial state (i), then after a 15V 15s voltage pulsing programming (ii), and finally with a -15V 15s voltage pulsing programming (iii). Scale bar, 4 μm. The normalized photocurrent intensity is indicated by the position of the dashed red line (iv). The photocurrent mapping is all performed under zero bias with λ=520 nm at 4.98 mW laser power. **c**, Typical I-V characteristics of the plasma-treated MoS_2 M/S/M photovoltaic detector under illumination, the I_{sc} switches from -6 nA to 1.5 nA and switches from 1.5 nA to 49 nA after the program of 100 negative pulses (-15V, 100 ms) followed by 50 negative pulses (−20 V, 100 ms). Then, the I_{sc} switches from 49 nA to 16 nA and from 16 nA to -11 nA after the program of 400 positive pulses (15V, 100 ms) followed by 700 positive pulses (15 V, 100 ms). **d**, Typical I-V characteristics of the pristine MoS_2 M/S/M photovoltaic detector under illumination, the I_{sc} remains constant after the program of 500 negative pulses (-15V, 100 ms) followed by 1000 negative pulses (−15 V, 100 ms). **e**, Performance statistics of 10 different reconfigurable MoS_2 M/S/M photovoltaic detectors showing their reconfigurabilities.

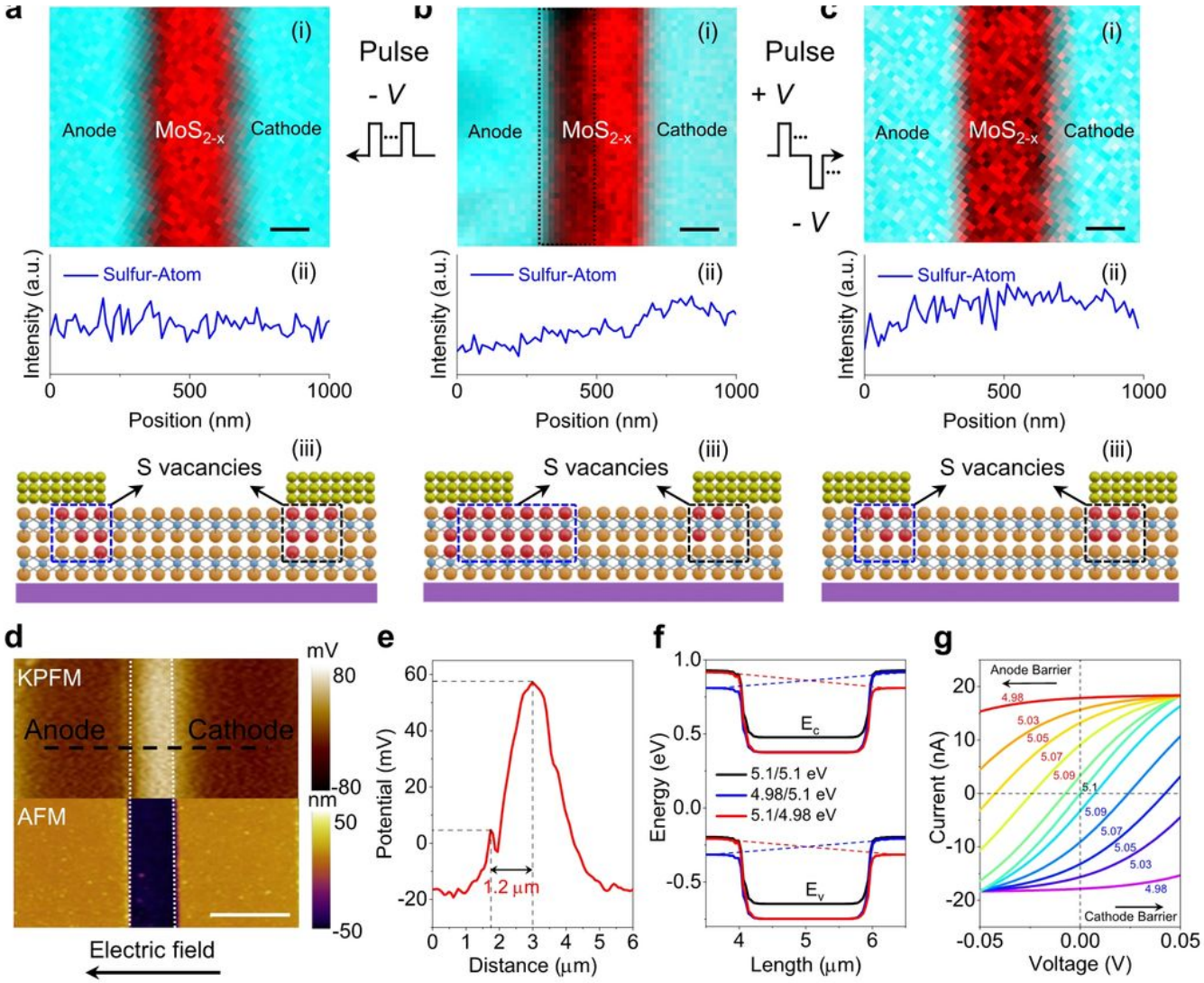

Figure 3. Sulfur vacancies migration and potential profile programming in the plasma-treated MoS_2 M/S/M photovoltaic devices. a-c, The WDS mapping of sulfur atoms distribution (i), elemental spectrum (ii), and schematic diagram (iii) of the reconfigurable MoS_2 photovoltaic detector at initial state **(a)**, after a negative pulse programming **(b)** and followed by a positive pulse programming **(c)**. WDS map shows migration of sulfur vacancies under electric pulse programming. Scale bar, 0.5 μm. Blue sphere: molybdenum, orange sphere: sulfur, golden sphere: metal, red sphere: sulfur vacancy. **d,** KPFM and AFM images for the reconfigurable MoS_2 M/S/M photovoltaic detector. Scale bar, 2 μm. **e,** The channel potential as a function of the position indicated by the dashed black line in panel d) shows a strong potential drop across the anode and cathode regions. **f,** Energy band diagrams for three Schottky barrier distributions in the TCAD simulation model. **g,** Variation of I_{sc} in the MoS_2 M/S/M photovoltaic detector as the anode and cathode potentials change in the TCAD simulation. The potential variation leads to changes in the polarity of I_{sc} in the M/S/M photovoltaic detector.

Figure 3

See above image for figure legend.

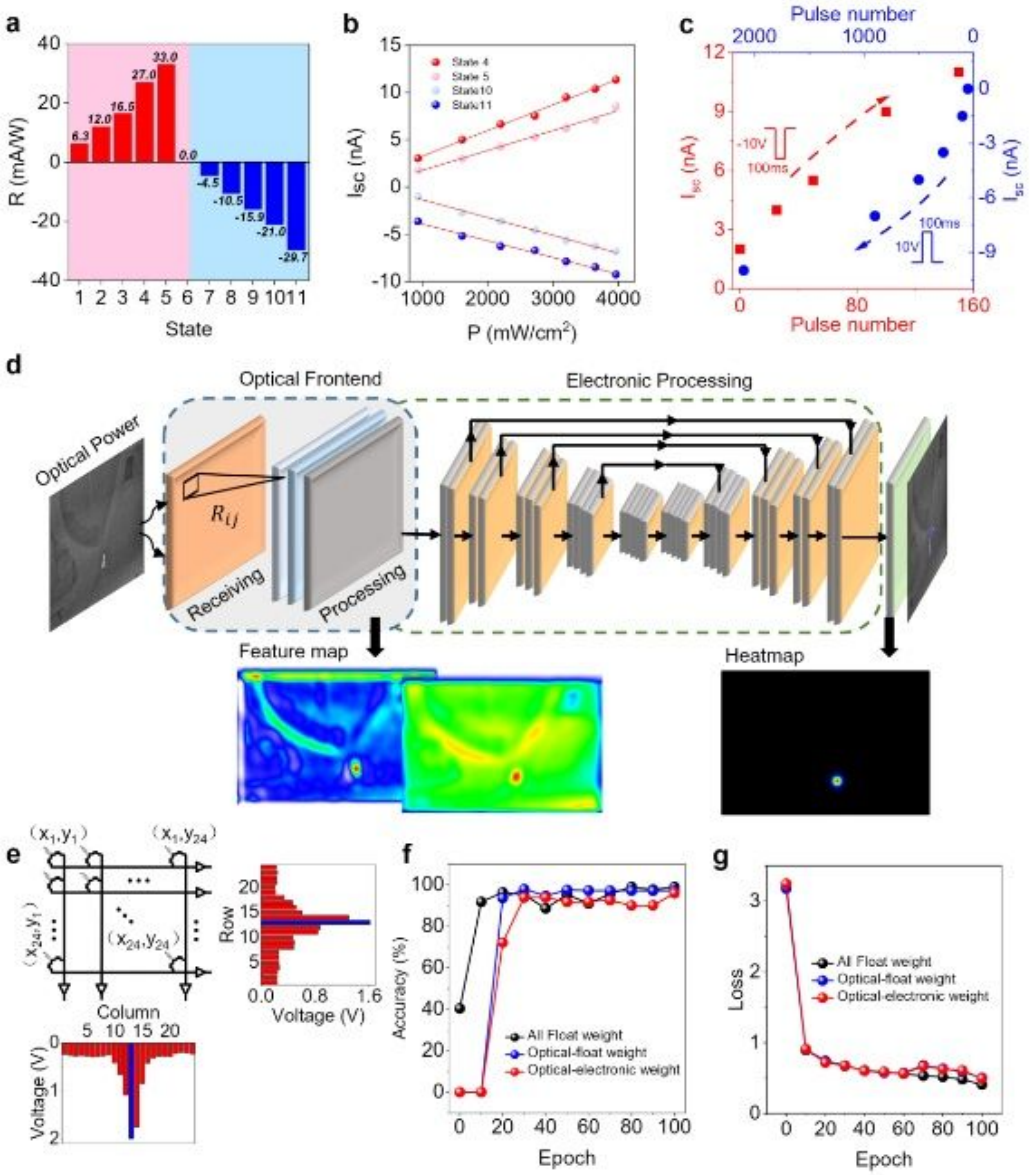

Figure 4. Object detection using MoS_2 M/S/M devices with reconfigurable and non-volatile responsivities. a, Eleven non-volatile responsivity states of plasma-treated MoS_2 M/S/M devices from a representative device. **b,** I_{sc} as a function of optical power density shows a highly linear relationship. **c,** Positive and negative I_{sc} obtained with different pulsing cycles (negative pulse, -10V 100 ms, positive pulse, 10V 100 ms). **d,** Artificial neural network structure for object detection that is divided into two stages -i.e. optical front-end and electronic back-end processing, the output of the object detection network is a heatmap, where peak in the heatmap corresponds to the object center, the size of the heatmap is 24× 24 in our experiments. **e**, Memristor crossbar arrays take the heatmap as input and output the coordinate (x, y) of the peak in the heatmap. The position of the object obtained from the memristor crossbar arrays, and the histogram graph show the experimental results (the number of rows and columns are both 24). **f,** Accuracy of all floats, optical-float, and optical-electronic weight for object detection. **g,** Training loss with three types of weight in the training process for object detection.

Figure 4

See above image for figure legend.

Supplementary Files

This is a list of supplementary files associated with this preprint. Click to download.

- SupplementaryInformationfinal.docx